Journal of Coastal Research	00	0	000–000	Coconut Creek, Florida	Month 0000

Assessing the Surface Radiation Balance and Associated Components in an Intertidal Wetland

Alejandro J. Vitale[†‡§]*, Sibila A. Genchi[§], and M. Cintia Piccolo[†§]

[†]Instituto Argentino de Oceanografía
Universidad Nacional del Sur (UNS)—CONICET
Bahía Blanca, Argentina

[‡]Departamento de Ingeniería Eléctrica y de Computadoras
Universidad Nacional del Sur (UNS)
Bahía Blanca, Argentina

[§]Departamento de Geografía y Turismo
Universidad Nacional del Sur (UNS)
Bahía Blanca, Argentina

www.cerf-jcr.org

www.JCRonline.org

ABSTRACT

Vitale, A.J.; Genchi, S.A., and Piccolo, M.C., 0000. Assessing the surface radiation balance and associated components in an intertidal wetland. *Journal of Coastal Research,* 00(0), 000–000. Coconut Creek (Florida), ISSN 0749-0208.

Knowledge of the surface radiation balance and associated components in intertidal wetlands is essential to the understanding of the ecosystem. The aim of this study is to assess the behavior of the radiation balance (or net radiation) and its components in a salt marsh environment (Bahía Blanca Estuary, Argentina), taking into consideration two different tidal conditions: nonflooded salt marsh (NFS) and flooded salt marsh (FS). *In situ* measurements were made during a 1-year period. An adequate measurement system to record meteorological and oceanographic parameters by using a floating structure was implemented. The results showed that the tide led to an increase of 5% in net radiation for a typical summer day (NFS = 3485 W m^{-2} d^{-1}; FS = 3663 W m^{-2} d^{-1}), while for a typical winter day, the net radiation under NFS and FS conditions was similar (NFS = –616 W m^{-2} d^{-1}; FS = –615 W m^{-2} d^{-1}) but showing differences throughout the day. With the purpose of strengthening the results, a spectral analysis using Fourier and wavelet transforms was performed on the net radiation and tide level time series.

ADDITIONAL INDEX WORDS: *Net radiation, tidal cycle, salt marsh, spectral analysis.*

INTRODUCTION

Solar radiation is the main energy input to the atmosphere–ground system. Surface radiation balance (SRB) involves complex feedback mechanisms at the atmosphere–ground interface. SRB determines the available energy for the non-radiative components of the heat balance at the Earth's surface (Marty *et al*., 2002) and for other energy-consuming processes like photosynthesis (Rosenberg, Blad, and Verma, 1983). Consequently, SRB is of great importance in many areas of physical, hydrological, and biological research.

SRB (or net radiation (R_n)) is defined as the difference between the incoming and outgoing radiation fluxes at the surface, including shortwave and longwave spectral regions; R_n (W m^{-2}) is determined as follows:

$$R_n = K\downarrow - K\uparrow + L\downarrow - L\uparrow = K\downarrow(1-\alpha) + L\downarrow - L\uparrow \qquad (1)$$

where, $K\downarrow$ and $K\uparrow$ are the incoming and outgoing shortwave radiation, respectively; $L\downarrow$ and $L\uparrow$ are the incoming and outgoing longwave radiation, respectively; α is the albedo. While incoming components of radiation balance are controlled by factors related to solar motion (*i.e*. latitude and season), cloudiness, aerosol loading, and atmospheric water vapor amount; outgoing components depend on ground surface characteristics (*i.e*. albedo, thermal emissivity, temperature, moisture, and soil properties).

SRB is variable in both spatial and temporal scales. The atmospheric conditions in combination with ground surface characteristics make it difficult to provide general rules of SRB. According to Ferreira *et al*. (2012), when the components in Equation (1) are considered individually, they may differ considerably from one area to another, even for equal R_n amounts. Numerous studies concerning SRB in different landscapes were conducted. For instance, SRB in urban areas was the focus of particular attention (*e.g*., Ferreira *et al*., 2012; Frey, Rigo, and Parlow, 2007; García Cueto *et al*., 2015; Offerle, Grimmond, and Oke, 2003; Sozzi *et al*., 1999). In other cases, several investigations focused on the SRB in diverse vegetation covers (*e.g*., Alados *et al*., 2003; Pieri, 2010; Samani *et al*., 2007; Sicart *et al*., 2004) or in topographically complex landscapes (*e.g*., Fritschen and Qian, 1990; Holst, Rost, and Mayer, 2005; Hong and Kim, 2008; Marty *et al*., 2002).

In coastal intertidal zones, the solar exposure is often dictated by tidal level (Crowell, Webster, and O'Driscoll, 2011). The strong horizontal flux driven by water movement complicates the exchange of matter and energy in these zones (Piccolo, 2009). Flood durations are long enough to perturb environmental conditions such as sediment temperature, saturation, *etc*. (Moffett *et al*., 2010). Hence, knowledge of the SRB and its components in these intertidal environments is crucial to the understanding of the ecosystem. Marine intertidal organisms are subjected to a variety of abiotic stresses, such as aerial exposure and wide ranges of temperature (Stillman and Somero, 2000), which are strongly related to both tide and solar radiation.

The surface balances (*e.g*., energy, water, carbon dioxide, *etc*.) between wetlands and the atmosphere are typically measured

DOI: 10.2112/JCOASTRES-D-17-00086.1 received 23 November 2017; accepted in revision 6 February 2018; corrected proofs received 5 March 2018; published pre-print online 4 April 2018.
*Corresponding author: vitale.alejandro@gmail.com

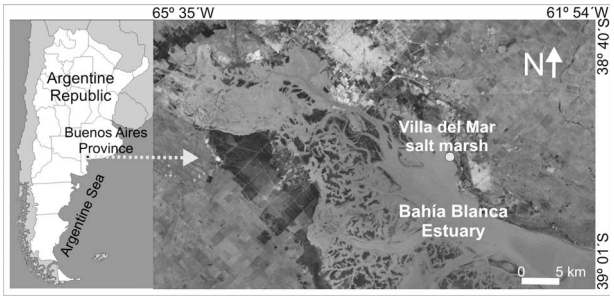

Figure 1. Location map of the study area (image from Google Earth).

during nonflooded conditions (Moffett *et al*., 2010). For example, the studies of Beigt, Piccolo, and Perillo (2008), Moffett *et al*. (2010), Silis, Rouse, and Hardill (1988), and Vugts and Zimmerman (1985) provided findings on heat–energy balances in different intertidal zones of the world, with attention on the tidal cycle (*i.e*. flooded and nonflooded conditions). However, it should be noted that the SRB and/or its components were investigated in an indirect way. Therefore, the aim of this study was to assess the behavior of the SRB and its components in a salt marsh, taking into consideration two different tidal conditions: nonflooded salt marsh (NFS) and flooded salt marsh (FS). The emphasis was put on quantifying the effect of the tide on the R_n and outgoing components of the SRB.

Field research was conducted in Villa del Mar salt marsh, in the NE of the Bahía Blanca Estuary (Buenos Aires province, Argentina) (Figure 1), which constitutes an ecological system, located in a subhumid (average annual humidity 60%; average annual rainfall = 635 mm) temperate (average annual temperature = 15.1°C) climate zone. The estuary is classified as mesotidal; the mechanical energy input into the system is produced by a semidiurnal tidal wave (Perillo *et al*., 2001). The average tidal range increases from the mouth (2.2 m) to the estuary head (3.5 m). The waves are characterized by a period not exceeding 2 seconds and a height of up 0.20 m for 70% of the time (Vitale, 2010). The salt marsh presents pure stands of *Spartina alterniflora* short form (González Trilla *et al*., 2009) and circular mounds of *Sarcocornia perennis*, colonizing the upper marshes (Perillo and Iribarne, 2003). Sediment granulometry indicates the predominance of a sandy silt texture (52% sand; 38% silt) (Vitale *et al*., 2014).

METHODS

Continuous and simultaneous measurements of meteorological and oceanographic parameters were made in the Villa del Mar salt marsh (Figure 2), in the framework of Coastal Environmental Monitoring Station (EMAC, 2018) network (http://emac.iado-conicet.gob.ar/). The period studied was from December 2008 to November 2009. The main equipment was installed in a position of the salt marsh that approximately 50% of the time is exposed to the atmosphere (*i.e*. NFS) and the remaining time is flooded by the tide (*i.e*. FS). With respect to FS condition, tides greater than 0.5 m were considered for analysis.

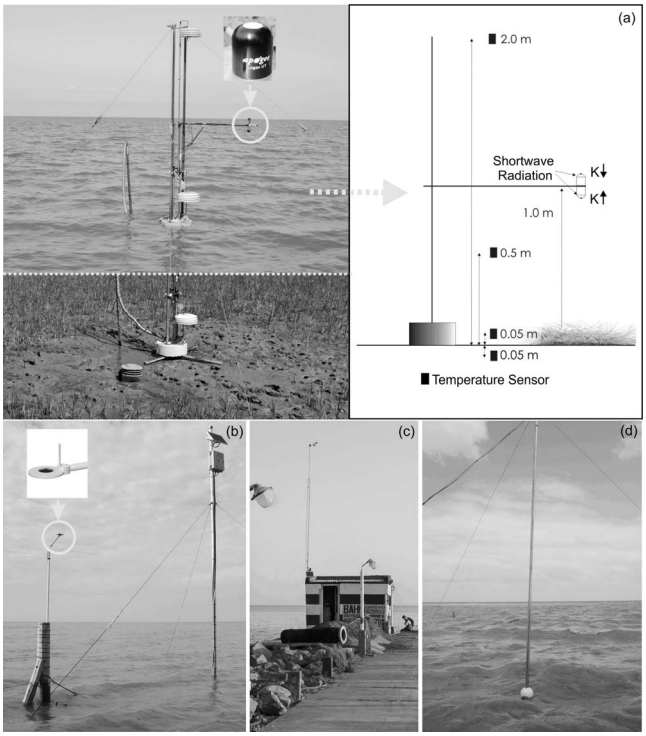

Figure 2. The used instrumentation: (a) Floating structure under flooded and nonflooded conditions, shortwave radiation, and temperature (sediment and air/water) sensors; (b) net radiation sensor; (c) weather station; and (d) magnetic wave and tide sensor.

The above-mentioned equipment consists of an innovative floating structure built in steel (buoy) in order to achieve a constant height above the surface (sediment or water) (Figure 2a). In addition, the floating system was designed to ensure a perpendicular orientation (to the surface) of the sensors. The equipment measures air temperature at 0.5 and 2 m and shortwave radiation at 1 m height above the surface (movable) (Figure 2a). Two pyranometers (Apogee, model SP-110; spectral range, 300–1100 μm) were placed opposite each other in the buoy for measuring $K\downarrow$ and $K\uparrow$. In the cases when solar zenith angle exceeded 80 degrees or $K\downarrow < 15$ W m^{-2}, the data were discarded. Temperatures at +0.05 m (air/water) and –0.05 m (sediment) were also measured close to the buoy (Figure 2a). Both sets of sensors were intercalibrated before the measurements. Measurements were recorded every 5 minutes.

A net radiometer (Kipp & Zonen, NR-Lite; spectral range 0.2–100 μm) was installed near the buoy, at the same tidal level as the pyranometers (Figure 2b). The radiometer calibrations were provided by manufacturer. R_n data were recorded every 5 minutes.

The weather station is located 150 m west of the buoy (Figure 2c). The station recorded relative humidity, air temperature, precipitation, barometric pressure, and wind speed and direction every 5 minutes. Also, wave (height and period) and tide level were recorded every 10 minutes (Figure 2d).

$L\downarrow$ was obtained as a residual term of the radiation balance (Eq. 1), as in similar studies (*e.g*., Stephens *et al*., 2011**;**

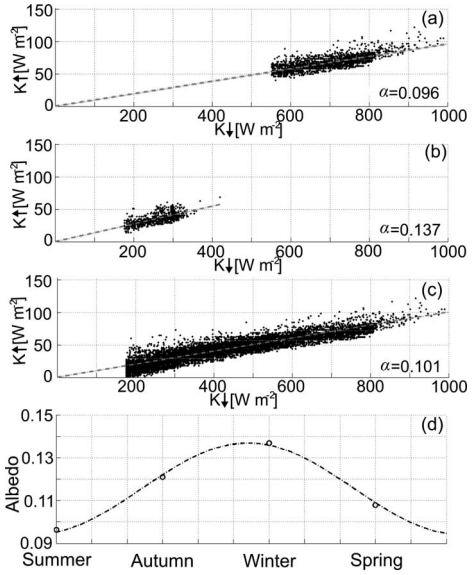

Figure 3. Correlation between $K\downarrow$ and $K\uparrow$ and the resultant albedo under NFS conditions for (a) summer, (b) winter, and (c) annual period. (d) Seasonal values of albedo; as can be seen, the curve is well fit to a sinusoidal function (See Eq. 5).

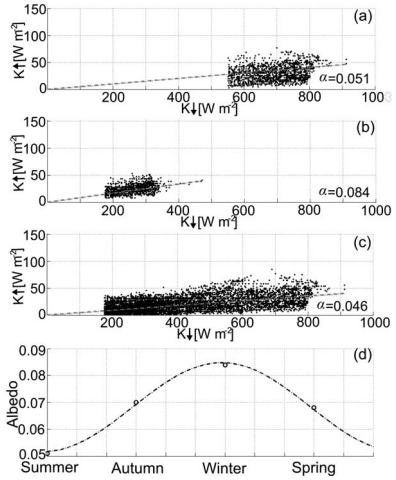

Figure 4. Correlation between $K\downarrow$ and $K\uparrow$ and the resultant albedo under FS conditions for (a) summer, (b) winter, and (c) annual period. (d) Seasonal values of albedo; as can be seen, the curve is well fit to a sinusoidal function (See Eq. 6).

Venäläinen, Solantie, and Laine, 1998), in the following way:

$$L\downarrow = R_n - K\downarrow + K\uparrow + L\uparrow \quad (2)$$

$L\uparrow$ was determined from measurements of surface (*i.e.* sediment or water) temperature using the Stefan-Boltzmann law, as follows:

$$L\uparrow = \varepsilon_s \sigma T_s^4 \quad (3)$$

where, ε_s is the thermal emissivity of the surface, σ is the Stefan-Boltzmann constant (5.67×10^{-8} W m^{-2} K^{-4}), and T is the surface temperature (sediment or water) (Figure 2a). Earth's surface is usually considered a grey body with a longwave emissivity in the range of 0.90 to 1, for example, from 0.90 (snow surfaces) to 0.98 (semiarid regions) (Garratt, 1994); in this case, ε_s is assumed to be 0.95 and 0.97 for FS (water) and NFS (sediment), respectively. Cloudiness is usually used as a general indicator that determines the atmospheric transmission of radiation (Jung *et al.*, 2016). Here, cloud cover (c, dimensionless) was determined by the following equation (Crawford and Duchon, 1999):

$$c = 1 - \frac{K\downarrow}{K\downarrow_t} \quad (4)$$

where, $K\downarrow_t$ is the theoretical incoming clear sky solar radiation, which depends on the time of day, Julian day, and latitude.

For the spectral analysis, fast Fourier transform (FFT) and wavelet transform methods were used. The former method was applied only for R_n, whereas the latter was applied for R_n and tide level. Unlike the FFT, the wavelet transform allows identification of not only spectrum of the frequencies but also their localization on the time axis. In addition, cross wavelet transform, as the extended usage of wavelet analysis, was applied to detect intercorrelations between R_n and tide level; both R_n and tide level data were subsampled to 1 hour. These methods complement each other, as will be shown later. The description and mathematical formulation of the wavelet methods are well outlined in the literature. All spectral analysis were generated using MATLAB.

RESULTS

The results of the R_n at the surface (NFS and FS conditions) and its associated components are described in detail below. Also, results in terms of R_n and tide level derived from spectral analysis are considered here.

Shortwave Radiation Characteristics

In the study area, the average $K\downarrow$ was 280 W m^{-2} (December 2008–November 2009), ranging from 383 to 195 W m^{-2} in summer and winter, respectively. The maximum recorded $K\downarrow$ reached 1069 W m^{-2} at 2 hours after midday in early summer. The average $K\uparrow$ was 40 W m^{-2}, ranging from 48 to 35 W m^{-2} in summer and winter, respectively. Figures 3 and 4 present the correlation analysis between the two shortwave components with the purpose of determining the albedo for both NFS (Figure 3) and FS (Figure 4) conditions. The annual albedo was 0.115 and 0.068 for NFS and FS, respectively. The seasonal albedo ranged from 0.096 (summer) to 0.137 (winter) for NFS and from 0.052 (summer) to 0.085 (winter) for FS. Seasonal values of albedo were well fit by a sinusoidal function (Figures 3d and 4d). Therefore, the monthly albedo for both NFS (Eq. 5; Figure 3d) and FS (Eq. 6; Figure 4d) conditions can be expressed as follows:

$$\alpha = -0.0213\text{sen}\left(m\frac{\pi}{6} + 1.3590\right) + 0.1155 \quad (5)$$

$$\alpha = -0.0165\text{sen}\left(m\frac{\pi}{6} + 1.1077\right) + 0.06825 \quad (6)$$

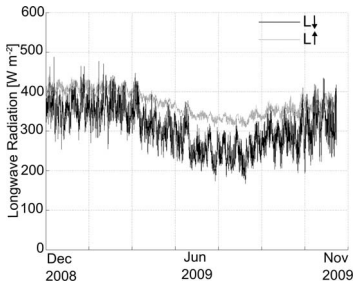

Figure 5. $L\downarrow$ and $L\uparrow$ components for the whole studied period (5-min time interval).

where, m is the number of the month (*i.e.* $1 \leq m \leq 12$, 1 = January).

Longwave Radiation Characteristics

Figure 5 shows both $L\downarrow$ (Eq. 2) and $L\uparrow$ (Eq. 3) components (values every 5 min) for the whole studied period. It should be remembered that $L\uparrow$ was adapted to NFS and FS conditions by using specific thermal emissivity. Because of the thermal inertia of the surface (either sediment or water), the fluctuation amplitude of the surface temperature is lower than the air temperature. This is clearly reflected in both $L\downarrow$ and $L\uparrow$ components (Figure 5). As expected, $L\downarrow$ and $L\uparrow$ components followed the same annual trend as the incoming solar radiation.

The average $L\downarrow$ was 357, 254, and 305 W m^{-2} in summer, winter, and annual period, respectively; the annual standard deviation was 54 W m^{-2}. These results were similar to those reported by Carmona, Rivas, and Caselles (2014), who carried out direct measurements of $L\downarrow$ (average $L\downarrow$ = 330 W m^{-2}, standard deviation $L\downarrow = 50$ W m^{-2}) in the central south-eastern area of Buenos Aires province (around 300 km from the study area). $L\uparrow$ was 418 and 341 W m^{-2} in summer and winter, respectively.

Cloud Cover

In this study, cloud cover is available only for daytime (see Eq. 4). Table 1 shows the monthly average cloud cover and the classification of sky conditions into four levels: clear, partly cloudy, mostly cloudy, and overcast. The monthly average cloud cover was 0.28, ranging from 0.19 (January) to 0.43 (May). Clear sky conditions accounted for 59% of the time (by averaging monthly values), while the remaining sky conditions accounted for 23% (partly cloudy), 12% (mostly cloudy), and 5.3% (overcast). During some months of winter and intermediate seasons (particularly May and September) the cloudiness increases, showing higher percentages of mostly cloudy and overcast sky conditions (Table 1).

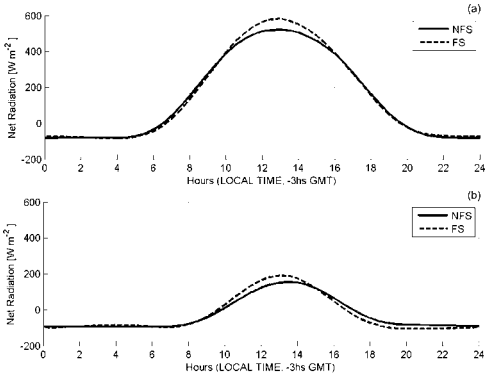

Figure 6. R_n for a typical day under NFS and FS conditions for (a) summer and (b) winter. The tide (*i.e.* FS condition) led to an increase in R_n at midday in both seasons.

Net Radiation at Different Tidal Levels

The average R_n in the salt marsh for the whole study period was 53 W m^{-2}. The seasonal average of R_n ranged from 132 to –11 W m^{-2} in summer and winter, respectively; this is the typical behavior in a temperate area. During daytime hours, the average R_n was 311 and 96 W m^{-2} in summer and winter, respectively, while during nighttime hours R_n was –70 and –90 W m^{-2} in summer and winter, respectively.

Figure 6 shows the behavior of the R_n for a typical summer and winter day, under NFS and FS conditions. Tidal effect on the R_n in both seasons can be clearly seen. The tide led to an increase of 5% in R_n for a typical summer day (NFS = 3485 W m^{-2} d^{-1}; FS = 3663 W m^{-2} d^{-1}) in average terms (Figure 7a). For a typical winter day, the R_n under NFS and FS conditions was similar (NFS = –616 W m^{-2} d^{-1}; FS = –615 W m^{-2} d^{-1}) (Figure 6b) but showing differences throughout the day.

In summer, the R_n reached a peak of 522 (NFS) and 585 W m^{-2} (FS) and a minimum of –79 (NFS) and –82 W m^{-2} (FS) (Figure 6a). The results showed a significant variation in R_n under NFS and FS conditions from 1000 to 1600 hours, being more marked at midday, in which R_n under NFS was lower than under FS. This is a consequence of the highest temperature reached by the sediment due to the maximum solar radiation (Vitale *et al.*, 2014) and the albedo effect; the albedo is greater for NFS ($\alpha = 0.096$) than for FS conditions by 88%, implying greater reflection of radiance. This behavior is inverted in the early hours of the morning (from 0630 to 0900 h). In this period, when R_n is governed by $L\uparrow$, the surface temperature plays a key role; since the water temperature is

Table 1. *Monthly cloud cover and classification of sky conditions.*

Sky Conditions	Jan	Feb	Mar	Apr	May	Jun	Jul	Aug	Sep	Oct	Nov	Dec
Average cloud cover	0.19	0.20	0.25	0.26	0.43	0.24	0.36	0.34	0.39	0.27	0.21	0.20
Clear sky (%)	77.4	78.6	67.7	43.3	32.3	63.3	38.7	48.4	43.3	64.5	75.0	76.2
Partly cloudy (%)	16.1	10.7	16.1	53.3	22.6	23.3	32.3	29.0	26.7	22.6	8.3	14.3
Mostly cloudy (%)	6.5	10.7	12.9	0.0	32.3	10.0	22.6	19.4	13.3	3.2	8.3	9.5
Overcast sky (%)	0.0	0.0	3.2	3.3	12.9	3.3	3.2	3.2	16.7	9.7	8.3	0.0

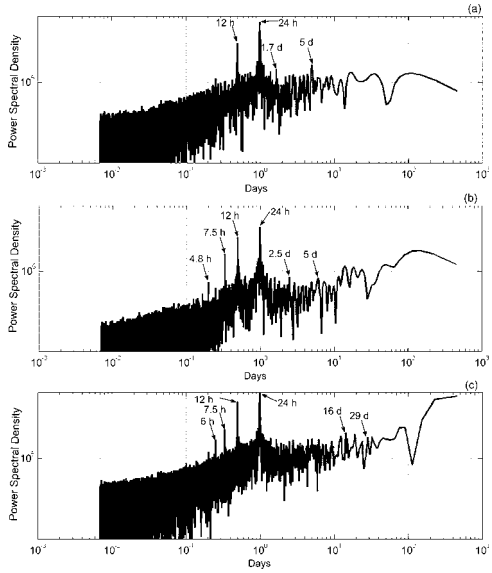

Figure 7. Fourier spectrum of R_n time series for (a) summer, (b) winter, and (c) annual period. (h = hour; d = day.) Two significant cycles of about 12 and 24 h are always observed, which are closely related to the tidal regime and to the diurnal variation of incoming solar radiation, respectively.

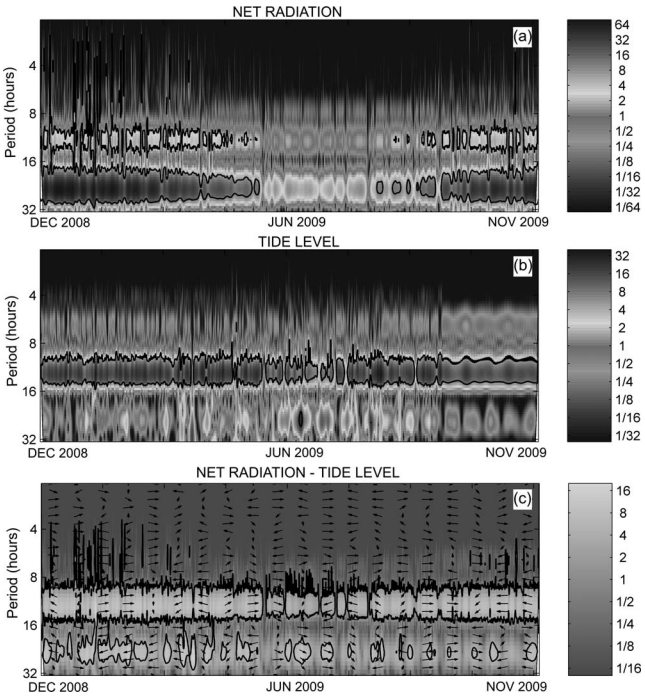

Figure 8. Wavelet analysis of R_n and tide level records from December 2008 to November 2009. Continuous wavelet transform of (a) R_n and (b) tide level. (c) Cross wavelet transform of R_n and tide level; well-defined areas (light colors) indicate strong relations between R_n and tide level at approximately 12 h.

higher than the sediment temperature (due to the cooling effect in the sediment produced by the minimum air temperature of the day) (Vitale *et al.*, 2014), the net radiative loss is slightly greater for FS than for NFS conditions (Figure 6a).

In winter, the R_n had a maximum of 155 (NFS) and 191 W m^{-2} (FS) and a minimum of –94 (NFS) and –104 W m^{-2} (FS) (Figure 6b). The plot showed that the R_n was greater (28%) under FS conditions than under NFS from 0930 to 1500 hours, when the water temperature remained below the sediment temperature; the smaller albedo of FS conditions also had an effect on the resultant R_n. Later, R_n became less negative (33%) for NFS from 1500 to 2400 hours, because the water temperature remains more constant (and higher) than the sediment temperature. The delayed effect of the resultant R_n for FS conditions can be clearly seen in Figure 6.

Spectral Analysis of Net Radiation and Tide Level

In order to carry out the spectral analysis of the *in situ* measured R_n and tide level, FFT (Figure 7) and wavelet transform (Figure 8) methods were used; however, FFT was applied only to R_n. With respect to FFT, two remarkable cycles were found in both summer and winter seasons: approximately 12 and 24 hours; the latter, and more important cycle, is thought to be due to the diurnal variation of incoming solar radiation; the remaining cycle is related to the tidal regime, which is dominated by the principal lunar semidiurnal constituent (M_2) (12.42 h). Peaks of about 5 and 7.5 hours are visible during winter (Figure 7b) (and annual period (Figure 7c)), which were associated to the longwave radiation rather than albedo, given mainly by the thermal responses of the surface under NFS and FS conditions throughout the day (Figure 7b). In addition, there are well-defined peaks in the energy spectrum near the 5-day cycle in both seasons and also between 10 and 20 days (annual period), which were probably triggered by the passage of synoptic systems (Figure 7b,c).

In accordance with the above FFT spectral analysis (Figure 7), the resultant wavelet power spectrum of the R_n (Figure 8a) showed a noticeable periodicity of about 24 hours (median value), related to incoming solar radiation. A second periodicity of about 12 hours (median value) was observed, related to semidiurnal tidal regime. In both cases, the power decreased in winter season (Figure 8a). The wavelet power spectrum of the tide level showed a clear periodicity with a period of about 12 hours (median value), as was expected (Figure 8b).

The cross wavelet analysis in figure 8c revealed well-defined areas (light colors) that indicate strong relations between the two time series. The cross power spectrum between R_n and tide level showed a common periodicity of about 12 hours, suggesting that the R_n is closely related to tide. Additionally, a quasi-periodic variation of about 24 hours was detected.

DISCUSSION

As was mentioned previously, the SRB determines the available energy for the nonradiative components of the heat balance (Marty *et al.*, 2002) and for other energy-consuming processes like photosynthesis (Rosenberg, Blad, and Verma, 1983). Knowledge of SRB and its components in intertidal wetlands is of great importance because it will contribute to

understanding the ecosystem function. In this regard, intertidal organisms are driven by the dynamics of the solar radiation and tide, which influence their behavior, survival, and growth. Thus, for instance, according to Mitbavkar and Anil (2004), the irradiance and tides are key factors for the control of vertical migration of benthic diatoms in a tropical intertidal environment.

For the first time, this study provides an assessment of the SRB and its components in a salt marsh under NFS and FS conditions. Regarding irradiance ($K\downarrow$), the seasonal average was 383 and 195 W m^{-2} in summer and in winter, respectively, as is typical in temperate regions. The annual average $K\downarrow$ was 280 W m^{-2}, while the annual average $K\uparrow$ was 40 W m^{-2}, indicating a positive annual shortwave radiation balance at the surface. The albedo was found to be higher for NFS, ranging from 0.096 (summer) to 0.137 (winter) for NFS and from 0.052 (summer) to 0.085 (winter) for FS. The results are similar to the findings reported by Moffett *et al*. (2010), who determined values (minimum) of albedo between 0.089 (NFS) and 0.073 (FS) for a salt marsh in San Francisco Bay, USA. Here, it is important to point out the development of the phytoplankton (dominated by diatoms) winter bloom in the Bahía Blanca estuary (Guinder, Popovich, and Perillo, 2009), which contributes to a decrease in albedo during FS conditions; in summer months, a phytoplankton peak abundance was also reported (Guinder *et al*., 2012). A strong explanation of the seasonal pattern under NFS and FS conditions is that, according to Fresnel's Law, at low solar altitudes (*i.e*. autumn–winter seasons) this direct radiation implies a higher albedo, and *vice versa* (Figures 3d and 4d). In addition, this pattern could not be explained by variations in the surface (specifically during nonflooded condition) due to the presence of perennial plant species.

The behavior of longwave components is related to the temperature; thus, $L\downarrow$ and $L\uparrow$ are highest in summer and lowest in winter seasons (Figure 5). The results indicated a continuous negative net flux. A perceptible gap between $L\downarrow$ and $L\uparrow$ (on average –87 W m^{-2}) was observed in winter months (Figure 5), in which $L\uparrow$ appears to be affected by the effects of tide on attenuation of the surface temperature, as was pointed out by Vitale *et al*. (2014). Tidal flooding has a general buffering effect on the variability of the sediment temperature (Serôdio and Catarino, 1999).

An assessment of cloud cover is necessary for radiation balance studies. Cloud cover reduces the $K\downarrow$; however, this effect is partly offset, or exceeded, by an increase in $L\downarrow$ (Screen and Simmonds, 2010). Hence, considering that the presence of clouds influences the SRB, a description of their cover was carried out. Cloud cover was estimated on the basis of measured $K\downarrow$, but this study did not include information on height and temperature of clouds, which influence significantly the $L\downarrow$. The monthly average cloud cover was 0.28, with highest values occurring during a few months of the year, in concomitance with rainy periods. This relatively low amount of cloudiness did not significantly affect the atmospheric radiation.

While the latitude of the site, season of year and time of day determine the amount of irradiance entering the ecosystem, the R_n also depends on the site conditions that characterize the ecosystem (Piccolo, 2009). As was already mentioned, the tidal cycle effectively influences the radiation balance by transiently altering the albedo, temperature, and emissivity. For a typical summer day, the tide led to an increase of the R_n by 5% (NFS = 3485 W m^{-2} d^{-1}; FS = 3663 W m^{-2} d^{-1}). The results showed a significant variation in the R_n for NFS and FS conditions mainly at midday, in which R_n under FS was higher than under NFS (Figure 6a). This means that there is available energy to achieve significant levels of photosynthesis, at flooded conditions, during midday, when irradiance levels are highest. For a typical winter day, the R_n under NFS and FS conditions was similar (NFS = –616 W m^{-2} d^{-1}; FS = –615 W m^{-2} d^{-1}), but with differences throughout the hours of the day (Figure 6b). Again, the R_n under FS was higher than under NFS, during midday hours. Therefore, the role of the tide in the variability of radiative net flux is of importance because the tide modifies both the surface temperature and albedo. This complex thermal behavior is in agreement with the fact that the intertidal species generally have high thermal tolerance (Stillman and Somero, 2000).

R_n and tide level were analyzed using spectral methods (FFT and wavelet transforms). The results agree with the abovementioned observations, giving complementary information. Spectral analysis applied to R_n and tide level time series revealed two clear periodicities of about 24 hours (Figures 7 and 8a) and 12 hours (Figure 8b) related to incoming solar radiation and to semidiurnal tidal regime, respectively. The most important result is that the Fourier and wavelet analysis of the R_n showed the role of tidal variability ($\approx$12 h) on R_n. Another important result is that the cross wavelet analysis strengthens the connection between R_n and tide level, showing a significant common periodicity of about 12 (Figure 8c).

CONCLUSIONS

An assessment of the SRB and its components in the Villa del Mar salt marsh (Bahía Blanca Estuary, Argentina) was carried out, taking into account the tidal cycle (*i.e*. NFS and FS conditions) as an essential part of this study. Continuous and simultaneous measurements of meteorological and oceanographic parameters were recorded during December 2008–November 2009. This research requires an adequate measurement system to continuously gauge the surface, that is, under NFS and FS conditions, which was achieved by equipping it with a floating structure.

This study contributes information about the factors determining radiation (shortwave and longwave) balance in an intertidal zone, providing the framework for further assessments and predictions of intertidal ecosystem functioning. Special attention should be directed toward trends in cloud cover within the global climate change context, which affects the radiation balance and influences the light conditions. Since climate change is expected to affect the sea level, salt marsh ecosystems will be impacted through changes in surface properties (*e.g*., albedo) and, hence, must be taken into account. Research efforts should include other specific physiological measurements, such as photosynthesis rate and evapotranspiration, among others, for future ecosystem modeling on intertidal environment.

ACKNOWLEDGMENTS

Partial support for the work dealing to this article was provided by grants from the CONICET, Agencia Nacional de Promoción Científica e Innovación Tecnológica, and Universidad Nacional del Sur.

LITERATURE CITED

Alados, I.; Foyo-Moreno, I.; Olmo, F.J., and Alados-Arboledas, L., 2003. Relationship between net radiation and solar radiation for semi-arid shrub-land. *Agricultural and Forest Meteorology*, 116(3–4), 221–227.

Beigt, D.; Piccolo, M.C., and Perillo, G.M., 2008. Surface heat exchanges in an estuarine tidal flat (Bahía Blanca estuary, Argentina). *Ciencias Marinas*, 34(1), 1–15.

Carmona, F.; Rivas, R., and Caselles, V., 2014. Estimation of daytime downward longwave radiation under clear and cloudy skies conditions over a sub-humid region. *Theoretical and Applied Climatology*, 115(1), 281–295.

Coastal Environmental Monitoring Station (EMAC), 2018. http://emac.iado-conicet.gob.ar/.

Crawford, T.M. and Duchon, C.E., 1999. An improved parameterization for estimating effective atmospheric emissivity for use in calculating daytime downwelling longwave radiation. *Journal of Applied Meteorology*, 38(4), 474–480.

Crowell, N., Webster, T., and O'Driscoll, N.J., 2011. GIS modelling of intertidal wetland exposure characteristics. *Journal of Coastal Research*, 27(6A), 44–51.

Ferreira, M.J.; de Oliveira, A.P.; Soares, J.; Codato, G.; Bárbaro, E.W., and Escobedo, J.F., 2012. Radiation balance at the surface in the city of São Paulo, Brazil: Diurnal and seasonal variations. *Theoretical and Applied Climatology*, 107(1), 229–246.

Frey, C.M.; Rigo, G., and Parlow, E. 2007. Urban radiation balance of two coastal cities in a hot and dry environment. *International Journal of Remote Sensing*, 28(12), 2695–2712.

Fritschen, L. and Qian, P., 1990. Net radiation, sensible and latent heatflux densities on slopes computed by the energy balance method. *Boundary-Layer Meteorology*, 53(1), 163–171.

García Cueto, R.; Santillán Soto, N.; Haro Rincón, Z.; and Ojeda Benítez, S., 2015. Parameterization of net radiation in an arid city of northwestern Mexico. *Atmósfera*, 28(2), 71–82.

Garratt, J.R., 1994. *The Atmospheric Boundary Layer*. Cambridge, UK: Cambridge University Press, 316p.

González Trilla, G.; Kandus, P.; Negrin, V.L.; Vicari, R., and Marcovecchio, J., 2009. Tiller dynamic and production on a SW Atlantic *Spartina alterniflora* marsh. *Estuarine, Coastal and Shelf Science*, 85(1), 126–133.

Guinder, V.A.; Molinero, J.C.; Popovich, C.A.; Marcovecchio, J.E., and Sommer, U., 2012. Dominance of the planktonic diatom *Thalassiosira minima* in recent summers in the Bahía Blanca Estuary, Argentina. *Journal of Plankton Research*, 34(11), 995–1000.

Guinder, V.A.; Popovich, C.A., and Perillo, G.M.E., 2009. Particulate suspended matter concentrations in the Bahía Blanca Estuary, Argentina: Implication for the development of phytoplankton blooms. *Estuarine, Coastal and Shelf Science*, 85(1), 157–165.

Holst, T.; Rost, J., and Mayer, H., 2005. Net radiation balance for two forested slopes on opposite sides of a valley. *International Journal of Biometeorology*, 49(5), 275–284.

Hong, J. and Kim, J., 2008. Simulation of surface radiation balance on the Tibetan Plateau. *Geophysical Research Letters*, 35(8), L08814. doi:10.1029/2008GL033613

Jung, Y.; Lee, H.; Kim, J.; Cho, Y.; Kim, J., and Lee, Y.G., 2016. Spatio-temporal characteristics in the clearness index derived from global solar radiation observations in Korea. *Atmosphere*, 7(4), 55. doi:10.3390/atmos7040055

Marty, C.H.; Philipona, R.; Fröhlich, C., and Ohmura, A., 2002. Altitude dependence of surface radiation fluxes and cloud forcing in the alps: Results from the alpine surface radiation budget network. *Theoretical and Applied Climatology*, 72(3), 137–155.

Mitbavkar, S. and Anil, A.C., 2004. Vertical migratory rhythms of benthic diatoms in a tropical intertidal sand flat: Influence of irradiance and tides. *Marine Biology*, 145(1), 9–20.

Moffett, K.B.; Wolf, A.; Berry, J.A., and Gorelick, S.M., 2010. Salt marsh–atmosphere exchange of energy, water vapor, and carbon dioxide: Effects of tidal flooding and biophysical controls. *Water Resources Research*, 46(10), W10525. doi:10.1029/2009WR009041

Offerle, B.; Grimmond, C.S., and Oke, T.R., 2003. Parameterization of net all-wave radiation for urban areas. *Journal of Applied Meteorology*, 42, 1157–1173.

Perillo, G.M. and Iribarne, O.O., 2003. Processes of tidal channel development in salt and freshwater marshes. *Earth Surface Processes and Landforms*, 28(13), 1473–1482.

Perillo, G.M.; Piccolo, M.C.; Parodi, E., and Freije, R.H., 2001. The Bahia Blanca Estuary, Argentina. *In:* Seeliger, U. and Kjerfve, B. (eds.), *Coastal Marine Ecosystems of Latin America*. Berlin and Heidelberg: Springer-Verlag, pp. 205–217.

Piccolo, M.C., 2009. Heat energy balance in coastal wetlands. *In:* Perillo, G.M.; Wolanski, E.; Cahoon, D.R., and Brinson, M.M. (eds.), *Coastal Wetlands: An Integrated Ecosystem Approach*. Amsterdam: Elsevier, pp. 211–226.

Pieri, P., 2010. Modelling radiative balance in a row-crop canopy: Cross-row distribution of net radiation at the soil surface and energy available to clusters in a vineyard. *Ecological Modelling*, 221(5), 802–811.

Rosenberg, N.J.; Blad, B.L., and Verma, S.B., 1983. *Microclimate: The Biological Environment*. New York: John Wiley, 528 p.

Samani, Z.; Bawazir, A.S.; Bleiweiss, M.; Skaggs, R., and Tran, V.D., 2007. Estimating daily net radiation over vegetation canopy through remote sensing and climatic data. *Journal of Irrigation and Drainage Engineering*, 133(4), 291–297.

Screen, J.A. and Simmonds, I., 2010. The central role of diminishing sea ice in recent Arctic temperature amplification. *Nature*, 464, 1334–1337.

Serôdio, J. and Catarino, F., 1999. Fortnightly light and temperature variability in estuarine intertidal sediments and implications for microphytobenthos primary productivity. *Aquatic Ecology*, 33(3), 235–241.

Sicart, J.E.; Pomeroy, J.W.; Essery, R.L.; Hardy, J.; Link, T., and Marks, D.A., 2004. A sensitivity study of daytime net radiation during snowmelt to forest canopy and atmospheric conditions. *Journal of Hydrometeorology*, 5(5), 774–784.

Silis, A.; Rouse, W.R., and Hardill, S., 1988. Energy balance of the intertidal zone of Western Hudson bay I: Ice free period. *Atmosphere-Ocean*, 27(2), 327–345.

Sozzi, R.; Salcido, A.; Saldana Flores, R.; and Georgiadis, T., 1999. Daytime net radiation parameterisation for Mexico City suburban areas. *Atmospheric Research*, 50(1), 53–68.

Stephens, G.J.; Wild, M.; Stackhouse, P.W. JR.; L'ecuyer, T.; Kato, S., and Henderson, D.S., 2011. The global character of the flux of downward longwave radiation. *Journal of Climate*, 25, 2329–2340.

Stillman, J.H. and Somero, G.N., 2000. A comparative analysis of the upper thermal tolerance limits of eastern Pacific porcelain crabs, genus *Petrolisthes*: Influences of latitude, vertical zonation, acclimation, and Phylogeny. *Physiological and Biochemical Zoology*, 73(2), 200–208.

Venäläinen, A.; Solantie, R., and Laine, V., 1998. Mean long-term surface energy balance components in Finland during the summertime. *Boreal Environment Research*, 3(2), 171–180.

Vitale, A.J., 2010. Modelado y Simulación del Balance Energético en Marismas. Bahía Blanca, Argentina: Universidad Nacional del Sur, Doctoral thesis, 250p.

Vitale, A.J.; Piccolo, M.C.; Genchi, S.A.; Delrieux, C.A., and Perillo, G.M., 2014. 3D numerical model of the thermal interaction between sediment–water–atmosphere. *Environmental Modeling & Assessment*, 19(6), 467–485.

Vugts, H.F. and Zimmerman, J.T., 1985. The heat balance of a tidal flat area. *Netherlands Journal of Sea Research*, 19(1), 1–14.